Earth Planets Space, **61**, 345–356, 2009

Resistivity and density modelling in the 1938 Kutcharo earthquake source area along a large caldera boundary

Hiroshi Ichihara*, Toru Mogi, Hideaki Hase, Tomonori Watanabe, and Yusuke Yamaya

Institute of Seismology and Volcanology, Hokkaido University, N10W8 Kita-ku, Sapporo, Japan

(Received April 5, 2008; Revised October 11, 2008; Accepted October 14, 2008; Online published March 3, 2009)

We present the crustal structure around the fault zone pertaining to the 1938 Kutcharo earthquake (M 6.0), northern Japan, to consider why large earthquakes have occurred around calderas. The study was based on gravity anomalies and magnetotelluric and direct-current (DC) electrical-resistivity survey data. The density structure obtained from gravity anomalies indicated that the fault plane corresponded to the main depression boundary of the Kutcharo caldera. The resistivity section, based on audio-frequency magnetotelluric surveys, indicated that the estimated fault plane was located along the boundary of resistivity blocks, which also corresponded to the depression boundary. A detailed resistivity section in the ruptured zone revealed by a DC electrical-resistivity survey showed a discontinuity of layers, implying cumulative fault displacements. These results indicate that the 1938 earthquake was an abrupt slip along the main depression boundary of the Kutcharo caldera. The most likely hypothesis pertains to fluid intrusion along the depression boundary. However, additional seismic and geodetic studies are required to identify other feasible earthquake mechanisms.

Key words: Magnetotellurics, gravity anomaly, DC electrical-resistivity survey, inland earthquake, Kutcharo caldera.

1. Introduction

Large earthquake events ($M > 5$) have often been reported around large volcanic calderas, such as the Long Valley caldera in the United States (e.g., Hill *et al*., 2003; Prejean *et al*., 2003), the Onikobe caldera in north-eastern Japan (Umino *et al*., 1998), and the Rabaul caldera in Papua New Guinea (Mori and McKee, 1987). Several studies have identified possible mechanisms for the occurrence of earthquakes around large calderas. For example, Umino *et al*. (1998) suggested that M 5.7 and M 5.9 earthquakes at the Onikobe caldera in 1996 were fault-slip earthquakes, which might have occurred along structural discontinuities around the caldera boundary. Because many inland earthquakes occurring in the upper crust have been considered abrupt slips within large discontinuous zones (e.g., Jackson, 1980; Kato *et al*., 2006), the large structural boundaries along calderas may also be important factors for the occurrence of earthquakes, suggesting that the caldera structure affects the occurrence of large inland earthquakes. However, the detailed relationship between caldera structures and fault activity has not yet been clarified.

Volcanic activity may be associated with the occurrence of large earthquakes around calderas as has been suggested for the Long Valley caldera (e.g., Julian, 1983; Savage and Cockerham, 1984; Prejean *et al*., 2003). For example, Julian (1983) indicated that several earthquakes in 1980 were caused by fluid injection into dykes through a mechanism explained by the compensated linear-vector dipole model. Savage and Cockerham (1984) suggested that dyke inflation generated tension across the vertical plane that became the ruptured surface of the earthquake swarm. This reduced the frictional stress on the rupture plane and perhaps triggered the slip that caused the swarms.

The 1938 Kutcharo earthquake (M 6.0) occurred within the Kutcharo caldera, which is located in the Akan-Shiretoko volcanic belt in the south-western Kurile arc of northern Japan (Fig. 1(a)). This area lies within one of the active inland earthquake areas of the Hokkaido district, the Teshikaga area, where eight large earthquakes ($M > 5$) occurred between 1938 and 1972 (Fig. 1(b)). The 1938 earthquake formed numerous rupture zones, mostly striking north-west to south-east (Fig. 1(c)). Based on the distribution of surface ruptures, the earthquake fault was estimated to be along a north-west–south-east strike azimuth between the Kushiro River and the Wakoto Peninsula (Tanakadate, 1938; Tsuya, 1938; Kato, 1940; Fig. 1(c)). Some of the ruptures showed left-lateral strike-slip and a maximum displacement of 2.5 m (Tsuya, 1938; Fig. 1(c)). Vertical displacements were also reported in the ruptures and formed a depression zone in the largest rupture zone (Fig. 1(c)). According to Tsuya (1938), the north-eastern side of the slip on the eastern flank of Maruyama subsided a maximum 0.8 m. A change in the lake level was also observed after the 1938 earthquake at the south part of the Kutcharo caldera. Tanakadate (1938) and Kato (1940) reported subsidence along, and upheaval, at the north-east side of the 1938 estimated fault (Fig. 1(c)). The vertical deformation

*Present address: Earthquake Research Institute, the University of Tokyo, 1-1-1 Yayoi, Bunkyo-ku, Tokyo 113-0032, Japan.

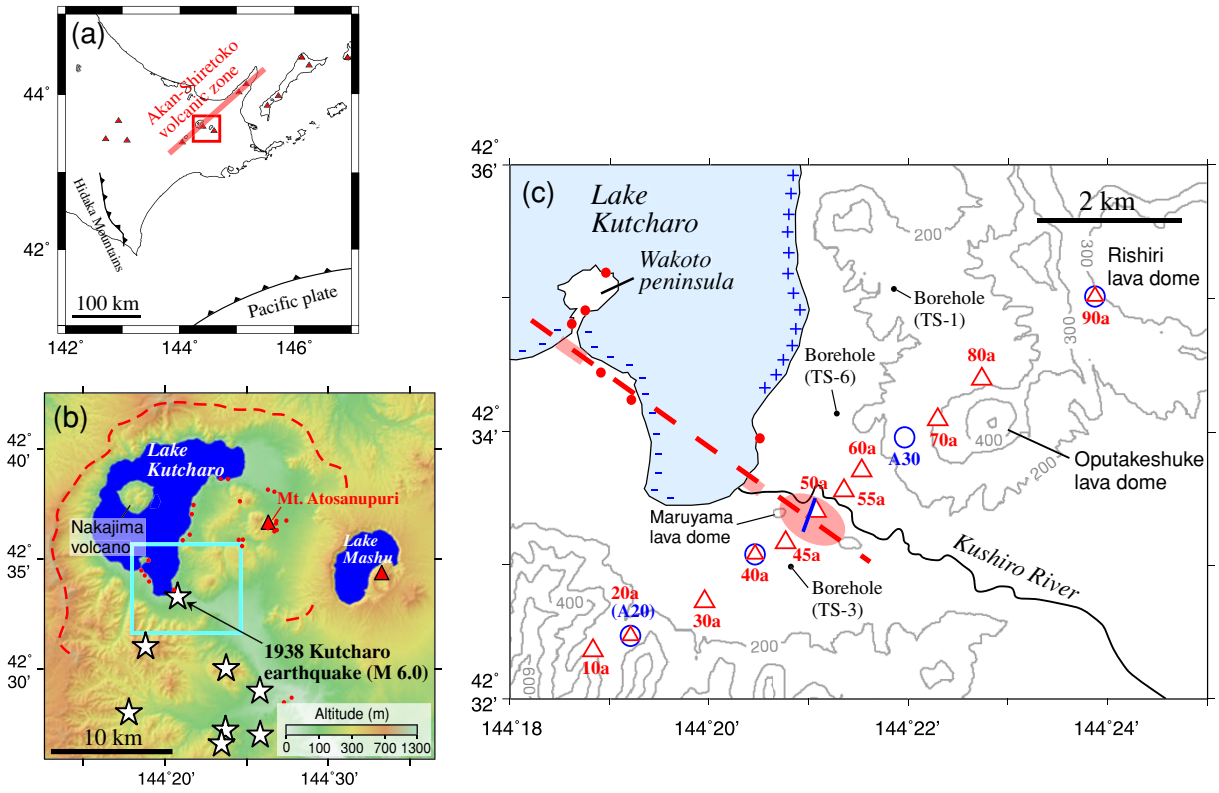

Fig. 1. (a) Tectonic setting around the study area. Red triangles denote active volcanoes. (b) Topography of the study area (red rectangle). Red dashed lines, Kutcharo caldera rim after Katsui (1962); stars, epicentres of the inland plate earthquakes that occurred between 1938 and 1967 (Suzuki and Hirota, 1973); red solid dots, hydrothermal activity. (c) Location of MT stations and rupture zones of the 1938 earthquake (light blue rectangle). Grey lines, altitude; pink areas, rupture zones; red dashed line, estimated fault of the 1938 Kutcharo earthquake (*M* 6.0; Tanakadate, 1938); blue plus, upheaval areas; blue minus, depression areas (Kato, 1940); Red dots, hydrothermal activity; circles, wideband MT stations; triangles, AMT stations; blue line, DC electrical resistivity imaging survey.

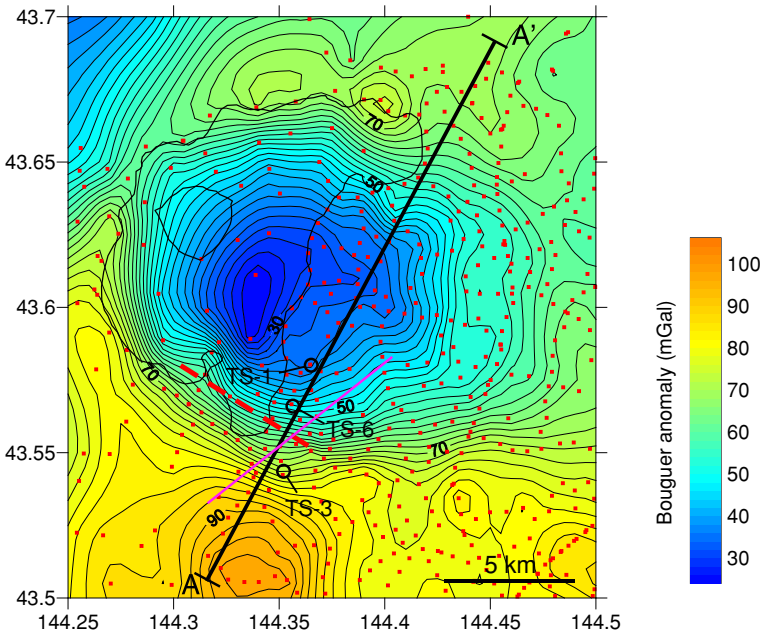

Fig. 2. Bouguer anomaly around Kutcharo caldera (assumed density, 2400 kg/m^3). Red squares, gravity stations; pink line, MT survey profile; red dashed line, estimated fault of the 1938 Kutcharo earthquake (*M* 6.0; Tanakadate, 1938).

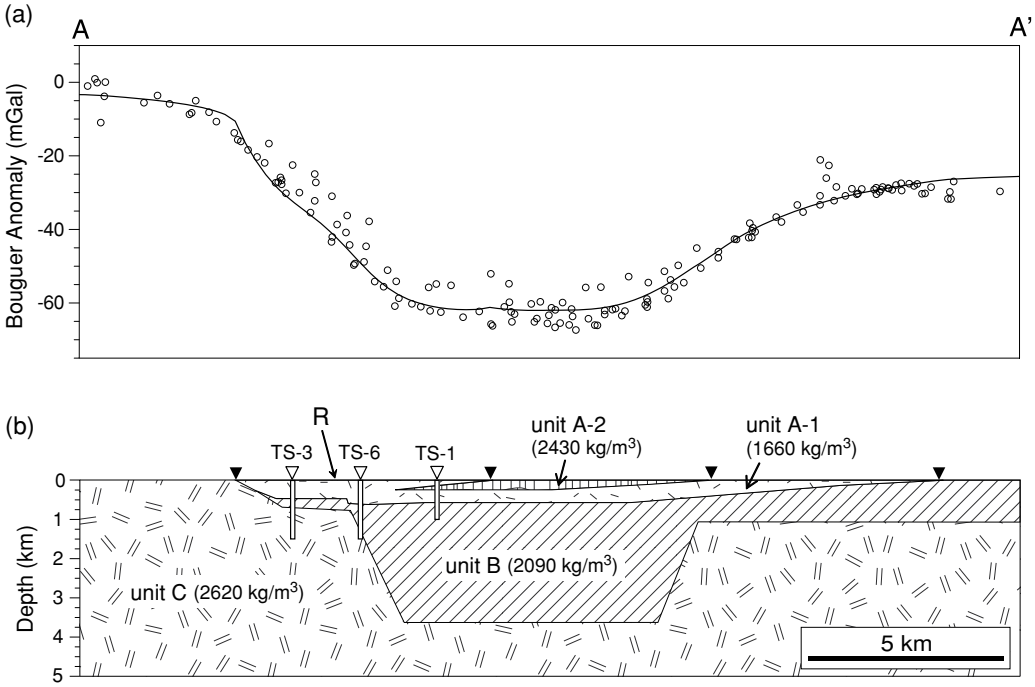

Fig. 3. (a) Bouguer anomaly along profile A–A′ in Fig. 2. Circles, observed gravity anomaly at a station within 3.0 km of the profile; solid line, calculated gravity anomaly of the final 2-D density model. (b) The final 2-D density model along profile A–A′. Inverted triangles, borehole site locations; inverted solid triangles, surface geological boundaries; R, rupture zone location of the 1938 Kutcharo earthquake.

indicated by the changing lake level seems to contradict that of the rupture displacement. Nevertheless, no quaternary fault activities have been identified around the study area. This may be due to the thickness of the pyroclastic flows and tuffs created by volcanic events that bury evidence of fault activity.

The activity around the Kutcharo caldera is divided into three stages: the precaldera, caldera-forming, and postcaldera stages (Hirose and Nakagawa, 1995). The precaldera stage activity (1.8–0.87 Ma) formed somma lavas between the rims of the Kutcharo caldera (Hirose and Nakagawa, 1995). In the caldera-forming stage (0.34 Ma–31 ka), numerous eruptions caused pyroclastic flows that formed the Kutcharo caldera (e.g., Katsui, 1962; Koshimizu and Ikushima, 1989). Postcaldera activity formed the Mt. Atosanupuri volcano and the lava domes denoted in Fig. 1(c), and this volcano has shown recent activity. Hydrothermal activity has also been identified, especially on the eastern side of the Kutcharo caldera (Fig. 1(b)).

Yokoyama (1958) reported a clear negative Bouguer anomaly in the Kutcharo caldera, in which the gravity was about 40 mGal lower at the centre of the caldera than at the rim. This implies a significant density anomaly around the Kutcharo caldera. Detailed investigations by density modelling could identify the geometry of the geological boundary, which may be related to fault activity. Therefore, we modelled the density structure using densely distributed gravity data. Surface geology and borehole data were used as constraints to obtain a robust density model.

We also conducted audio-frequency magnetotelluric (AMT) surveys and modelled the electrical-resistivity distribution. Imaging of the resistivity distribution is effective for estimating fluid distribution because it depends on porosity as well as the salinity and interconnectivity of the fluid (e.g., Archie, 1942). In addition, resistivity imaging is particularly sensitive to clay minerals, such as montmorillonite, produced by alteration because they significantly reduce resistivity of the host rock (e.g., Takakura, 1995), and detecting such clay minerals supports the presence of hydrothermal activity (e.g., Nurhasan *et al.*, 2006). Thus, resistivity imaging helps identify fluid distribution in volcanic areas, which may be related to the occurrence of earthquakes, such as the earthquake swarms in the Long Valley caldera. In addition, resistivity reflects geological heterogeneity (e.g., Park and Wernicke, 2003), so we also interpreted the resistivity structure to identify the geological structure.

Additionally, we performed a two-dimensional (2-D) direct-current (DC) electric resistivity survey within the ruptured zone of the 1938 fault, which detects vertical displacement from fault activity when resistive or conductive layers are distributed beneath fault zones (e.g., Suzuki *et al.*, 2000). With this approach, the historical activity along the 1938 fault, which is not known, can possibly be clarified.

2. Density Structure

2.1 Bouguer anomaly

We calculated the Bouguer anomaly around the Kutcharo caldera using gravity data reported by Yokoyama (1958), the Japan Geothermal Energy Development Centre (1980), Ichihara *et al.* (2006), Yamamoto and Ishikawa (2004) and Hasegawa *et al.* (2006). We assumed that the density for the Bouguer and the terrain corrections were 2400 kg/m^3 because Yamamoto and Ishikawa (2004) estimated a 2400±130 kg/m^3 optimum surficial density based on a method developed by Murata (1993) using Akaike's

Table 1. Summary of the lithology and petro-physical properties of the boreholes drilled by NEDO (1985). The density value is the average of measured core samples from four boreholes drilled in the caldera. The P-wave velocity (V_p) and resistivity are from the velocity found by electrical logging (100 cm normal) at borehole TS-3. The resistivity range is based on standard deviations in logarithms of the resistivity. Calculations were based on the average of V_p and density listed in the left columns, and 0.25 was assumed for Poisson's ratio.

Unit	Lithology	Age	Density (kg/m^3)	V_p (km/s)	Young's module (GPa)	Resistivity (ohm-m)
Unit A-1	Pumice and Pyroclastic deposits	Quaternary	1660±320	2.00	6.1	68–370
Unit A-2	Andesitic lavas	Quaternary	2400±130	—	—	—
Unit B	Tuff and volcanic breccias	Pliocene –Quaternary	2090±280	2.74	14.1	18–83
Unit C	Altered andesite and pyroclastic rocks	Middle Miocene	2620±120	3.88	32.6	290–980

Bayesian Information Criterion (ABIC).

The Bouguer anomaly showed a steep gradient around the 1938 estimated fault (Fig. 2). At the north-east side of the fault, the estimated anomaly was 60 mGal lower than that at the south-west side, and the gravity gradient exceeded 10 mGal/km near the estimated fault. This considerable gravity variation indicated a large density contrast or a deeply extending density boundary. In addition, the strike of the gravity contours was parallel to the strike of the 1938 estimated fault. These results implied a relationship between the fault plane and density heterogeneity caused by the caldera formation.

2.2 Two-dimensional density modelling

Using 2-D forward processing (Talwani *et al.*, 1959), we modelled the density structure along the A–A′ profile to identify the density distribution around the ruptured zones (Fig. 2), which cross the estimated fault of the 1938 earthquake. The observed Bouguer anomalies within 3 km from the profile are presented in Fig. 3(a).

Based on samples from three boreholes drilled to a depth greater than 1 km by the New Energy and Industrial Technology Development Organization (NEDO, 1985), the geology of the Kutcharo caldera was categorised into units A-1, A-2, B, and C in the model (Table 1). The geometry of the boundaries between each unit was estimated in the model by assuming a fixed density within each unit (Table 1). Three boreholes drilled by NEDO near the profile (TS-1, TS-3 and TS-6) provided information on the depth of the unit boundaries. The boundary depths for unit A-1/B were 545, 697, and 507 m in boreholes TS-3, TS-6, and TS-1, respectively. The boundary depths for unit B/C were 742 and 1366 m in boreholes TS-3 and TS-6, respectively. Unit A-2 (Atosamupuri somma lava) was between depths of 416 and 610 m in borehole TS-1. These boundary depths and the surface geological boundary (Matsunami and Yahata, 1989; Fig. 3(b)) were used as a model constraint.

Features of the final density model (Fig. 3(b)) and their validity are as follows:

1) The boundary depth between units A-1 and B did not vary significantly around the rupture zones of the 1938 earthquake, which is validated by the borehole data (545, 697, and 507 m in boreholes TS-3, TS-6, and TS-1, respectively).
2) The boundary depth between units B and C changed sharply around borehole TS-6; it was over 3500 m deep at the north-east side and approximately 900 m at the south-west side of the rupture zone. Borehole TS-3 limited the sharp change in depth. If the depth of the boundary between units B and C changes gradually, then the boundary depths between A-1/B and B/C must significantly exceed the constraint depths of boreholes TS-3 and TS-6.
3) The bottom depth of unit B was estimated to be 3500 m, but two reasons suggest that the true depth was probably deeper. First, the density contrast between units C and B (530 kg/m^3) should decrease with depth because unsolidated sediment (unit B), but not solidated rock (unit C), is compacted with depth. A smaller density contrast requires a deeper boundary between units B and C. Second, although Bouguer anomalies clearly implied a three-dimensional (3-D) structure, we assumed a 2-D structure in this modelling (Fig. 2). The 2-D analysis assumed that density anomalies (units A-1, A-2, and B) are distributed infinitely along the strike zone; however, if the low-density area has a limited distribution along the strike, the bottom depth of unit B should be deeper than shown by the 2-D model. The deeper boundary indicates that the gradient of the unit B/C boundary under the ruptured zone is steeper than that indicated by the final density model.
4) Because the density models that followed the constraints explained in 1) and 2) did not completely fit the observed gravity data, the calculated gravity was slightly lower than the observed gravity around borehole TS-6 (Fig. 3(a)). This inconsistency may be alleviated when the compaction of units A and B is further investigated or a 3-D model is developed.
5) No borehole data were available for the unit boundaries at the north-east of borehole TS-1, so the depths were not determined.

3. Resistivity Structure Derived from Magnetotelluric Observations

3.1 Magnetotelluric survey and data processing

AMT surveys were conducted across the rupture zone of the 1938 earthquake fault at 10 sites in May and November 2006 (Fig. 1(c)). A time series of the MT data were recorded using the MTU2000 system manufactured by Phoenix Geophysics, Ltd. (Toronto, ON, Canada). The electric fields were measured at all sites using orthogo-

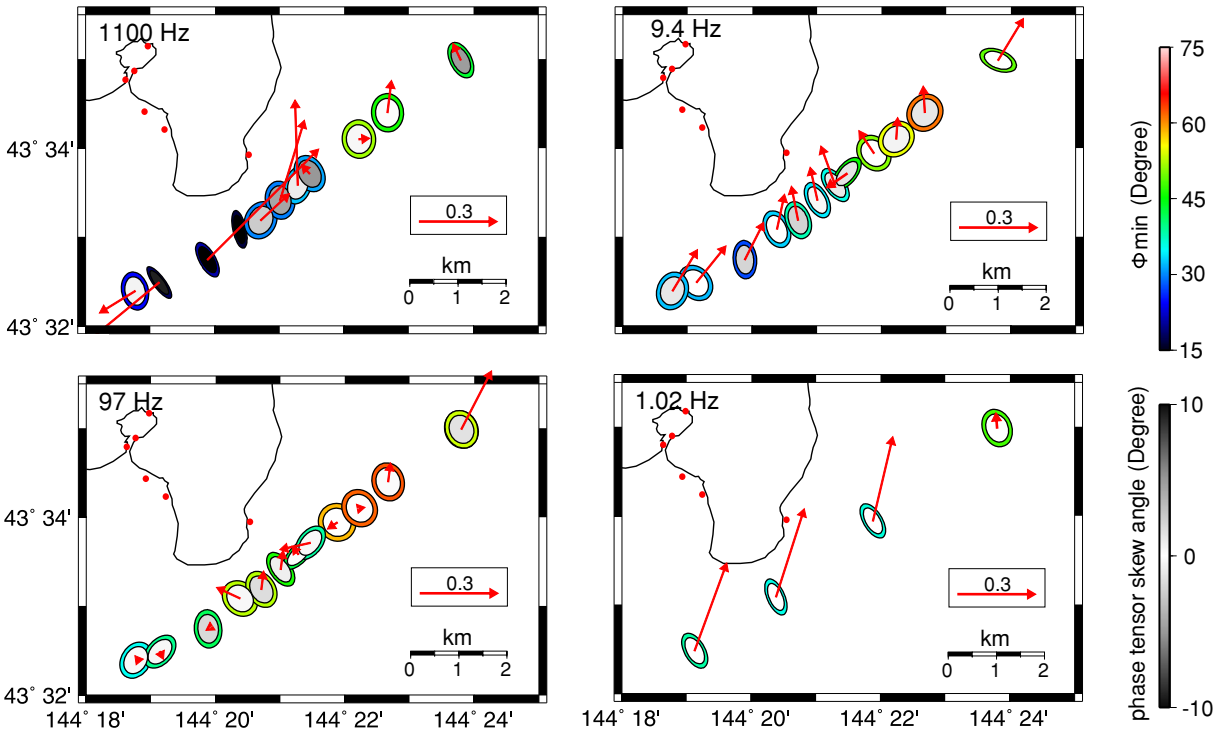

Fig. 4. Phase-tensor ellipses and Parkinson's induction vectors (1100, 97, 9.4, and 1.03 Hz). Colour scales of the outer ellipse, Φ_{min} skew angles; grey scales of the inner ellipse, phase-tensor skew angles; red arrows, induction vectors; red dots, hydrothermal activity. AMT and wideband MT data (Ichihara *et al.*, 2006) were used for the analyses of 1100, 97, 9.4 Hz, and 1.03 Hz, respectively.

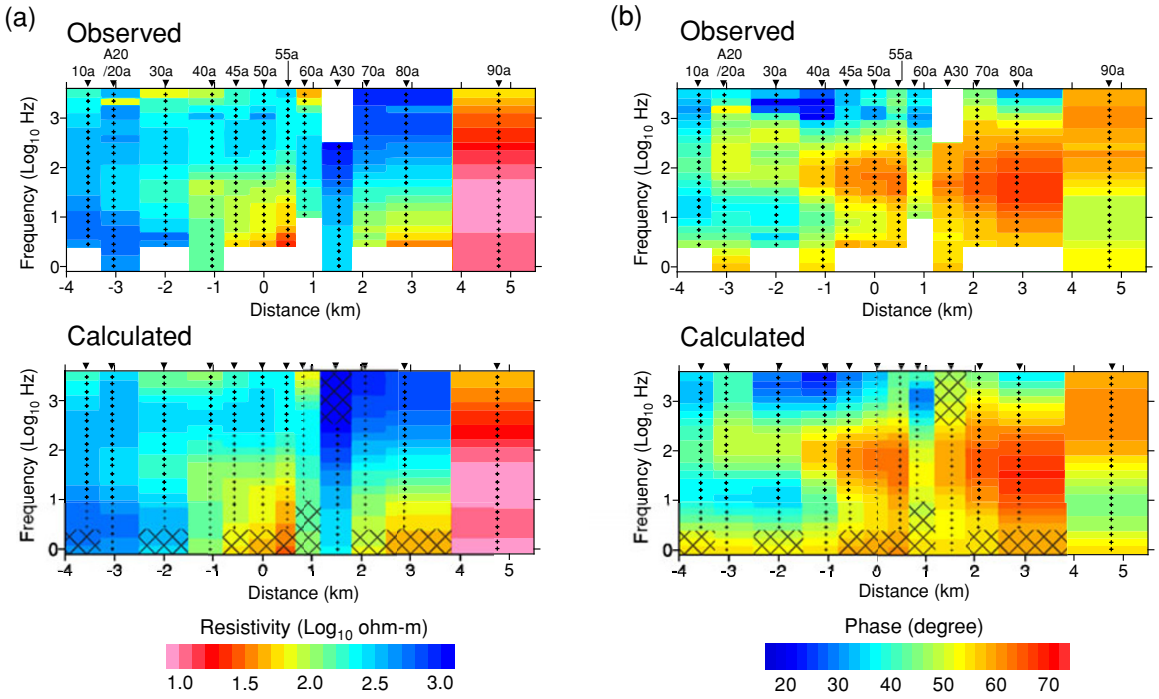

Fig. 5. Pseudo sections of the observed and calculated apparent resistivity and impedance phase for the MT inversion. Black dots, data used for the inversion procedure.

nal dipoles with Pb-$PbCl_2$ electrodes attached at both ends. The magnetic fields at all sites were measured using three orthogonal-induction coils. Wideband magnetotelluric data were also acquired at stations 40a and 90a using induction coils oriented for wideband sensing.

The recorded AMT time-series data were converted into impedance tensors in the frequency domain through a cascade decimation technique (Wight and Bostick, 1980). The frequency of the converted impedance for the AMT data ranged from 3300 to 0.35 Hz. High-quality data were obtained at most sites, but the lower frequency band for the AMT impedance (<2 Hz) was not well identified, espe-

cially for sites 10a, 30a, 55a, 70a, and 80a. In addition, we did not obtain impedances lower than 10 Hz at site 60a. The impedances in the so-called dead bands (5000–1000 Hz) were also not well determined at some sites. Wideband MT data at sites 40a and 90a (Fig. 1(c)), and A20 and A30 (Ichihara *et al.*, 2006) were converted into impedance tensors between 320 and 0.00055 Hz through the same process used for the AMT data. High-quality data were obtained at all sites and for most frequency bands.

3.2 Estimation of the 2-D strike azimuth and dimensionality of the MT data

The magnetotelluric-phase tensors (Caldwell *et al.*, 2004) and Parkinson's induction vectors were calculated to verify two-dimensionality and to determine the 2-D azimuth for the inversion. Phase tensor is an important tool to recognise the dimensionality of the subsurface structure. The phase tensor is defined as

$$\mathbf{\Phi} = \mathbf{X}^{-1}\mathbf{Y},$$

where $\mathbf{X}$ and $\mathbf{Y}$ are the real and imaginary components of the impedance tensor ($\mathbf{Z}$), respectively. A significant advantage is that phase tensor is not affected by galvanic distortion. A phase tensor is written in the form

$$\mathbf{\Phi} = \mathbf{R}^T(\alpha - \beta)\begin{bmatrix} \Phi_{\max} & 0 \\ 0 & \Phi_{\min} \end{bmatrix}\mathbf{R}(\alpha + \beta),$$

where $\Phi_{\max}$, $\Phi_{\min}$ and β are co-ordinate invariants and $\mathbf{R}(\theta)$ is a rotation matrix. The phase-tensor ellipse is the graphical expression of the phase tensor in which the major axis ($\Phi_{\max}$) and minor axis ($\Phi_{\min}$) of the ellipse depict the principal axes and the tensor values. The orientation of the major axis is specified by the angle $\alpha - \beta$. In the 2-D case, the major axis of the phase tensor is aligned parallel or perpendicular to the strike of the regional resistivity distribution. The phase-tensor skew angle, β, measures asymmetry of the phase response. For the detailed explanations, see Caldwell *et al.* (2004).

The azimuths of $\Phi_{\max}$ in the phase-tensor ellipses were mostly directed to the same azimuth as the MT profile (N55°E–S55°W) or its perpendicular azimuth (Fig. 4). Because $\Phi_{\max}$ and $\Phi_{\min}$ varied within the profile, the 2-D strike azimuth seemed to be oriented N35°W–S35°E. Based on the above two possibilities, the induction vectors (Parkinson's vectors) support the N35°W–S35°E azimuth as the 2-D strike (Fig. 4). Therefore, N35°W–S35°E was adopted as the strikes of the 2-D inversions. However, the induction vectors near the 1938 earthquake rupture zone oriented toward the north at 1100–9.4 Hz (Fig. 4). These features indicate the existence of a 3-D conductor in the northern part of the 1938 earthquake fault zone. The unsalted water of Lake Kutcharo was excluded as a candidate for the 3-D conductor.

3.3 Two-dimensional inversion of the MT data

After the impedances were rotated into the estimated 2-D azimuth, the apparent resistivity and phase in the frequency band between 3300 and 1 Hz were inverted using the 2-D inversion code developed by Ogawa and Uchida (1996). Pseudo sections of the data using the inversion and sounding curves of sites 40a and 55a are described in Figs. 5 and 6, respectively. The inversion code estimates the model based on the ABIC least-squares method and comprehensively evaluates the root-mean-square (RMS) misfit between the observed and calculated impedance, the model smoothness and static shifts. Impedances in lower frequency bands (<1 Hz) were not used for the inversion for the following reasons. First, the low frequency data at all of the wideband MT sites were affected by a large phase-tensor skew angle exceeding 10° and anomalous off-diagonal phases exceeding 90° (Ichihara *et al.*, 2006). Second, a NE–SW azimuth of the regional strike of eastern Hokkaido district (Satoh *et al.*, 2001) is not consistent with strike of our profile.

We used only the TM-mode impedances for the inversion for the following reasons. High phases around 100 Hz at sites 40a–55a also indicated a conductor around this area (Fig. 5). However, induction vectors oriented to the northwest between 1100 and 9.4 Hz (Fig. 4) implied that the conductor had a 3-D geometry. Ledo *et al.* (2002) and Siripunvaraporn *et al.* (2005) tested the 2-D inversion for a section in which a synthetic 3-D structure conductor was distributed in and out of the survey line, similar to the situation in this study. When the 3-D conductor is out of the profile, Siripunvaraporn *et al.* (2005) showed a phantom of the 3-D conductor among the inversions using TM, TE, and TM + TE mode impedances. However, Ledo *et al.* (2002) showed that the phantom is not clear in the TM + TE mode inversion compared to the TM mode inversion. Thus, TM + TE mode data seemed to be appropriate in our situation. When the 3-D conductor is in the profile, Siripunvaraporn *et al.* (2005) showed that inversions using only TM-mode impedances identified an appropriate structure, whereas inversions using only the TE mode or the TM + TE modes produced a strong phantom conductor beneath the true 3-D conductor. Ledo *et al.* (2002) also indicated that the TM mode was superior to the TM + TE data. Therefore, whether the 3-D conductor is in or off the profile determines the appropriate mode. Because resistivity logging in TS-3 showed a conductor in the profile between a depth of 500–700 m (NEDO, 1985; Fig. 1(c)), the conductor seemed to be distributed in the profile. Therefore, the TM mode was preferable for the inversion.

The inversion was started from a 100-ohm-m homogeneous half-space model. A 5% error floor in the apparent resistivity and phase was applied. The observed impedances were mostly explained by the inversion procedure (Fig. 5). The RMS misfit in the initial model (16.92) was reduced to 2.50 in the final iteration. The inverted resistivity section (Fig. 7) showed the following features:

1) A conductive body was imaged under the ruptured zone (C1, 10–30 ohm-m). The C1 conductor was required to explain large phases over 60° that were observed around 100 Hz at sites 40a–55a.
2) The C2 conductor (3–20 ohm-m) was distributed around the north-eastern edge of the profile, where hydrothermal activities have been observed (Fig. 1(b)). Low apparent resistivity at site 90a (Fig. 5) clearly indicated the C2 conductor.
3) A resistive area was imaged below 1000 m at the south-west side of the 1938 Kutcharo earthquake rup-

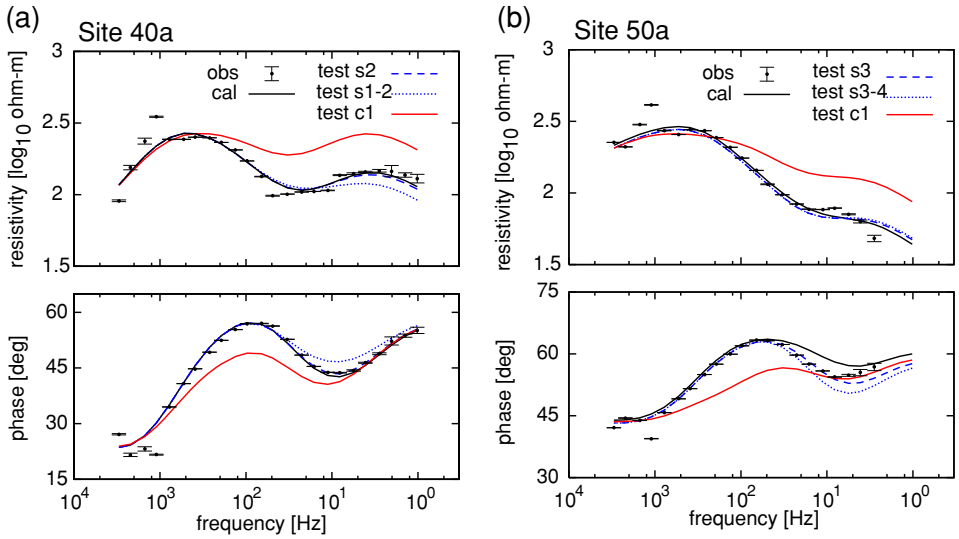

Fig. 6. Observed and calculated sounding curves for the apparent resistivity and phase of sites 40a and 55a. Dots with error bars, observed apparent resistivity and phase of TM mode; black solid line, inverted model; coloured lines, hypothetical model.

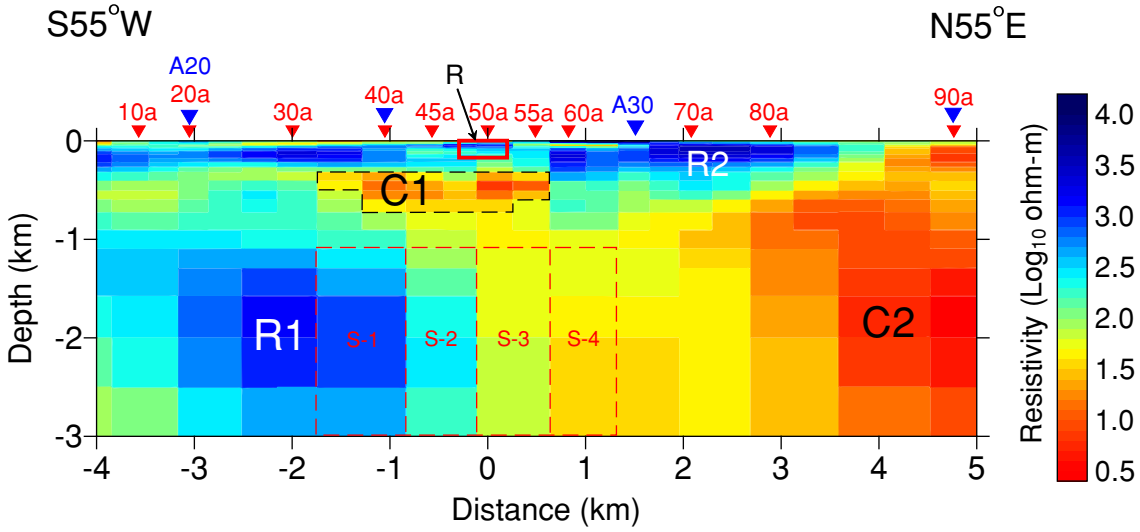

Fig. 7. Inverted 2-D resistivity image along the MT profile crossing the rupture zone of the 1938 Kutcharo earthquake (*M* 6.0). Red rectangle, location of the DC electrical survey in Fig. 8; R, location of a 1938 Kutcharo earthquake (*M* 6.0) rupture zone.

ture zone (R1, 500–1000 ohm-m). High apparent resistivity and low phase between 1 and 10 Hz at sites 10a, 20a/A20, A30 and 40a required the R1.

4) The resistive zone (R2) was detected from the surface to a depth of 200–300 m at the eastern part of the profile. R2 obviously corresponded to unit A-2 consisting of andesitic lavas.

Resistivity logging at TS-3, drilled near site 40a, measured a resistivity of 40–300 ohm-m in unit A (0–545 m of depth), 10–50 ohm-m in unit B (545–742 m) and 100–500 ohm-m in unit C (>742 m; Fig. 8). The inverted resistivity image was consistent with the vertical resistivity variations measured in borehole TS-3 (Fig. 8). Thus, the inverted image seemed to be reliable around borehole TS-3.

3.4 A sensitivity test of the inverted resistivity structures

The final inverted resistivity model from the MT data showed a conductive body under the rupture zone (C1, 20–50 ohm-m; Fig. 7). The sensitivity test confirmed the existence of the C1 conductor. Based on the final model, C1 is hypothesised to have been converted to 100 ohm-m (Fig. 7). The responses provided by the hypothetical model were significantly inconsistent with that of the final model and the observed 100 Hz at sites 40a–55a (Fig. 6). The RMS error of the hypothetical model increased from 2.50 to 4.84 in the final model.

The position of the boundary between R1 and the moderate resistivity zone was also important to the caldera structure and the 1938 earthquake, but the location is tenuous because the C1 conductor covered this area. Thus, we tested the sensitivity of the location with four hypothetical models. First, the S-2 region of the final resistivity model

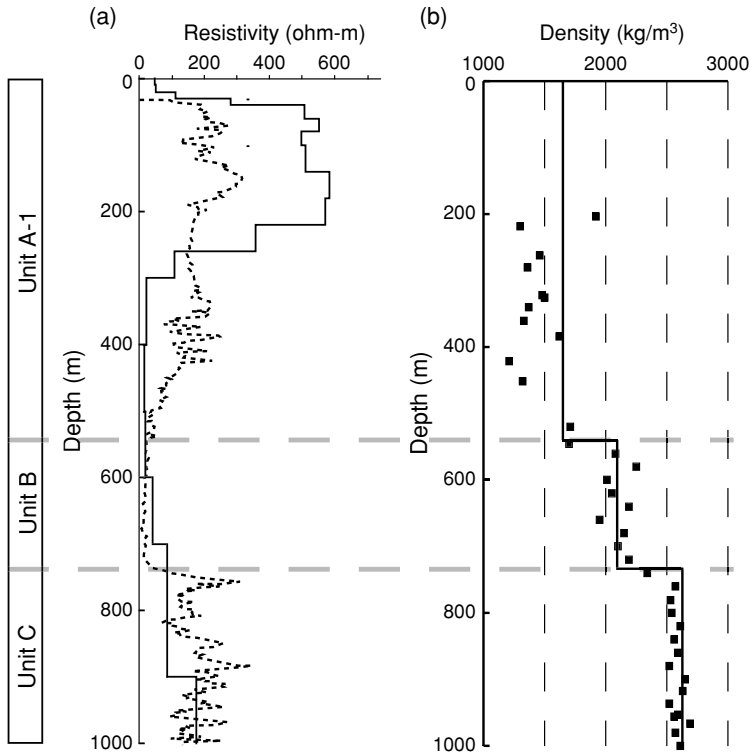

Fig. 8. Measured and modelled resistivities and densities along borehole TS-3 (NEDO, 1985). The location of the borehole is shown in Fig. 2. (a) Dotted lines, logged (25 cm normal) resistivity from the 2-D inversion; solid lines, estimated resistivity. (b) Dots, core sample wet density; solid line, estimated density (Table 1).

(Fig. 7) was filled with 50 ohm-m. The response produced by this hypothetical model was almost the same as the final model at all sites (response at site 40a is drawn with a blue dashed line in Fig. 6(a)). The second model indicated that a region between S-1 and S-2 was filled with 50 ohm-m. The model response showed significantly higher phases of around 10 Hz and lower apparent resistivity (<3 Hz) compared to the final model and the observed data (a blue dotted line in Fig. 6(a)). These results indicate that high resistivity was required at S-1 but possibly not at S-2. For the third hypothetical model, the S-3 region in Fig. 7 was filled with 300 ohm-m. These responses explained the sharp phase undulations of around 10 Hz at sites 50a and 55a compared to the final model (blue dashed line in Fig. 6(b)). The impedances at the other sites were almost the same as the final model. Finally, the S-3 and S-4 regions were filled with 300 ohm-m. The results differed significantly from the observed data and the third hypothetical model. Tests three and four indicated sharp resistivity changes between S-3 and S-4, but the smoothness constraint did not allow convergence into a sharp structure. Consequently, the location of the R1 margin was around S-2, S-3, and S-4, and the sharper resistivity boundary may have been distributed at the R1 margin.

4. DC Electrical Survey Around the Ruptured Zone

To reveal the detailed resistivity structure around the 1938 earthquake rupture zone, we performed a 2-D DC electrical-resistivity survey in November 2006. We laid a 490-m transect as an AMT survey line with 50 electrodes near site 50a (Fig. 1(c)). Then, DC electrical resistivities were measured from 748 combinations of transmitting and receiving dipoles in Wenner and Eltran arrays by using electrical-resistivity imaging instruments manufactured by Chiba Electronics Co. Interelectrode spacing (a) varied from 10 to 160 m. The sensitive zone of the Wenner array was concentrated at the dipole centres but was narrow along the horizontal direction. In contrast, the Eltran array had a relatively high sensitivity at the horizontally wide area but had reversed sensitivity at the outside of the dipole system. Both arrays had weaker sensitivity at areas deeper than a. Pseudo sections of the observed apparent resistivities are shown in Fig. 9. The observed apparent resistivity data were inverted to a 2-D resistivity image using the numerical inversion code developed by Uchida (1991). The inversion started from the 100 ohm-m homogeneous half-space model. An excellent fit of the observed data and the calculated pseudo sections was noted (Fig. 9). The RMS misfit was reduced from 46.6 to 1.34 in the final iteration.

Several features were recognised in the inverted resistivity section under the 1938 earthquake rupture zone (Fig. 10). One was a deep (>100 m) high-resistivity body (R3, <1000 ohm-m) found at the south-west side of the rupture zone. Because R3 was not found in the north-east side of the rupture zone, a thickness of the R3 resistive body greater than 30 m indicates that more than 30 m of vertical movement occurred along the 1938 earthquake fault. Past activity along this plane may have been supported by an approximately 10-m vertical offset, distributed around 50-m depth, between the relatively low resistivity anomalies of C3 and C4. The 10-m offset is not precise because the

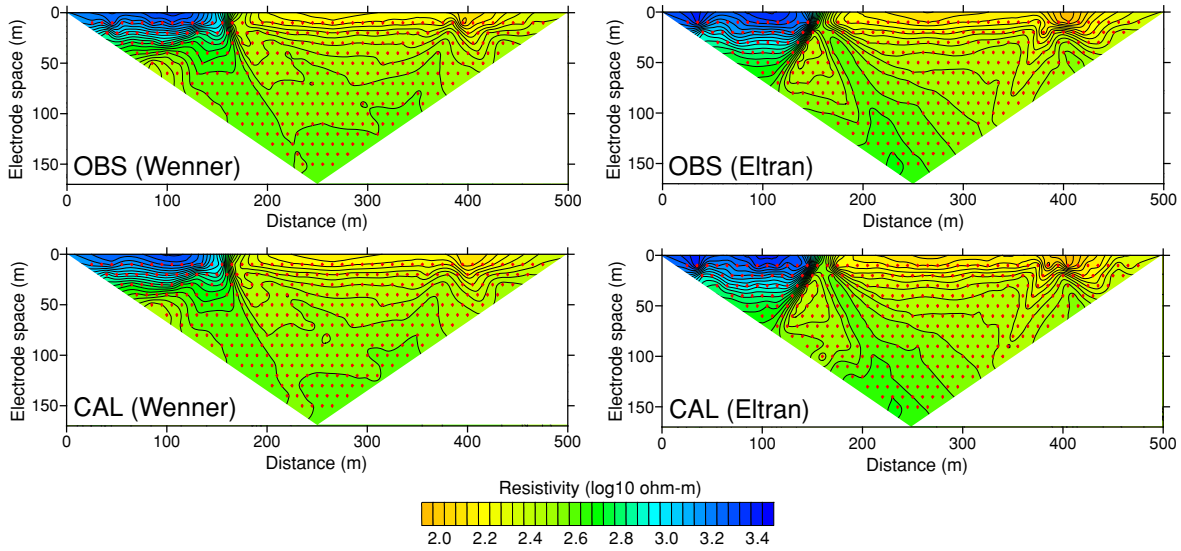

Fig. 9. Pseudo sections of the observed and calculated apparent resistivity phase for the DC electrical survey.

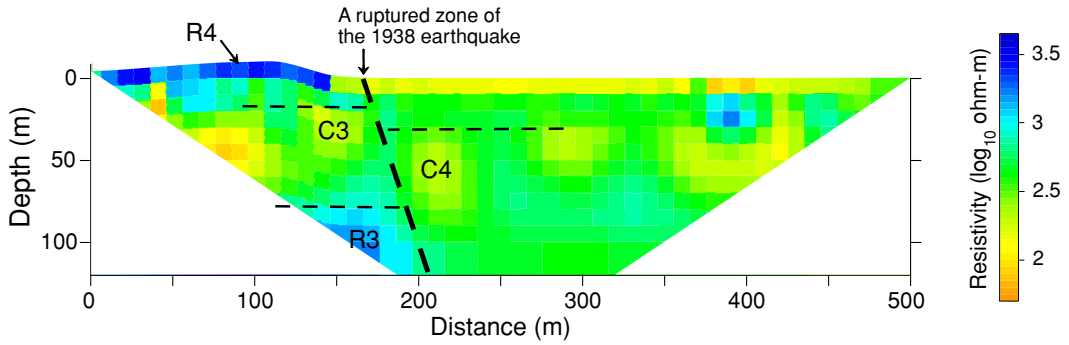

Fig. 10. DC resistivity image around the fault zone of the 1938 Kutcharo earthquake (6.0). A rupture zone created by the earthquake was reported near the 170-m point (Tsuya, 1938).

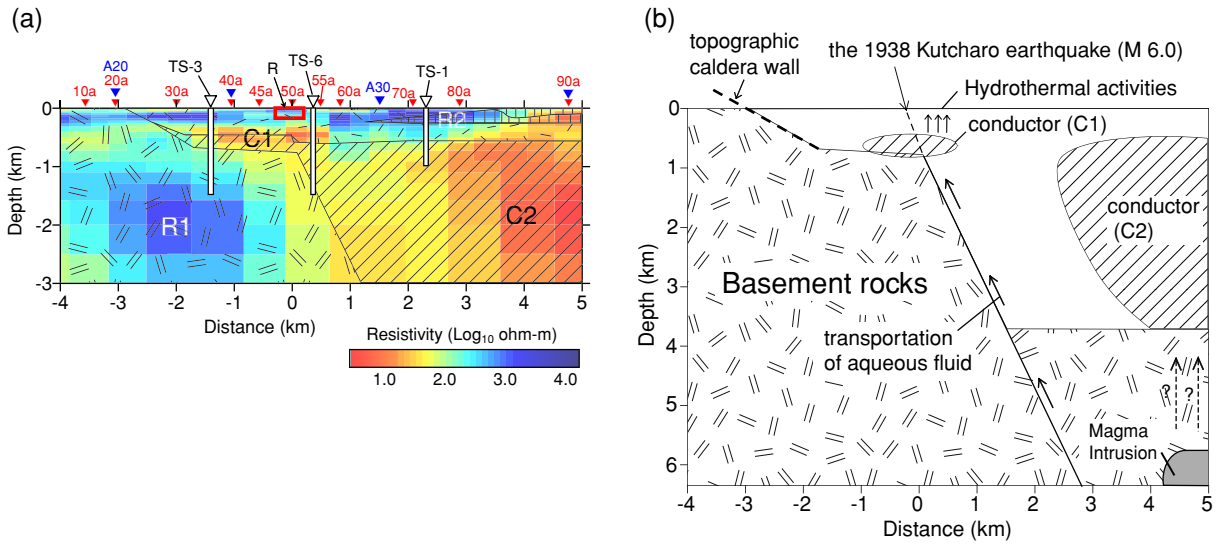

Fig. 11. (a) Comparison of the density and resistivity structure. The image created by the black mesh marks denotes the final density model in Fig. 3. The colour image describes the resistivity structure in Fig. 6 projected to profile A–A′ in Fig. 2. (b) A simultaneous image of the Kutcharo caldera and the estimated fault of the 1938 Kutcharo earthquake (*M* 6.0) along the same profile as shown in (a).

block size of the resistivity model was 10 m; however, it is thought to be adequately large compared to the vertical displacement caused by the 1938 earthquake (0.8 m; Tsuya, 1938). The lack of R3 on the north-east side and the offset between C3 and C4 may indicate subsidence at the north-east side as a result of repeated earthquake activity. These offsets are consistent with the vertical displacement of the 1938 earthquake surface ruptures. However, the changes in lake level after the 1938 earthquake indicate subsidence along or on the south-west side and upheaval at the north-east side of the ruptured zone (Kato, 1940; Fig. 1(c)). Detailed surveys, such as a fault trench, are required to clarify the fault movements.

A resistive zone (R4) was also identified immediately below the surface near the Maruyama dome at the south-west side of the profile. Because the area around the Maruyama lava dome has a higher elevation, R4 was probably associated with Maruyama lava.

5. Discussion

5.1 Interpretation of resistivity and density structures

The well-log (TS-3) drilled by NEDO (1985) provided information on the lithology, density, and resistivity of the site (Fig. 8). Based on this borehole data and other references, the calculated density and resistivity models can be interpreted as follows.

The final inverted resistivity model from the MT data showed a conductive body under the rupture zone (C1, 20–50 ohm-m; Fig. 7). The sensitivity test confirmed the existence of the C1 conductor. The C1 resistivity (10–30 ohm-m) was consistent with the logging resistivity of boreholes TS-3 and TS-6. A comparison of the resistivity between the final model and the TS-3 logging data is shown in Fig. 8. Montmorillonites were identified in core samples obtained near the C1 conductor (NEDO, 1985). Because montmorillonite significantly reduces the resistivity of host rock (e.g., Takakura, 1995), C1 is interpreted as a montmorillonite-rich zone and implies hydrothermal activity under the rupture zone because they are commonly produced by hydrothermal alteration. The C1 conductor seems to be distributed toward the north-west of the profile, but not the south-west side because the induction vectors pointed north at 1100, 97, and 9.4 Hz near C1 (Fig. 4). Significant hydrothermal activity has been recognised around Mt. Atosanupuri as well as along the 1938 estimated fault (Fig. 1(b, c) and Fig. 4), implying that the C1 conductor along the 1938 fault was produced by hydrothermal alteration. The margin of the depression zone may have been a path for water that subsequently induced the C1 hydrothermal alteration.

The magma intrusion has been estimated to be about 6 km deep at 2 km north of site 90a (Fig. 11(b); Geographical Survey Institute, 2006). In addition, hydrothermal areas and an active volcano (Mt. Atosanupuri) are distributed at the surface of the magma-intruded zone (Fig. 1(b)), suggesting that the C2 conductor was produced in association with these activities.

Unit C (Ikurushibe formation) consists mainly of andesite and tuff breccias, most of which are altered in the core samples. The Ikurushibe formation is assumed to be the lowermost layer among the outcroppings of the Neogene basement rocks in the Teshikaga area (Matsunami and Yahata, 1989). NEDO (1985) and Koshimizu and Kim (1986) suggested that the fission and track ages of the Ikurushibe formation are 13.1 and 7.9–8.2 Ma, respectively. The resistivity logging showed high resistivity (290–980 ohm-m; Table 1) in unit C. The inverted resistivity from the AMT survey along borehole TS-3 revealed high resistivity consistent with the logged data (Fig. 8), indicating that the resistive zone (R1) corresponded to unit C. In addition, the spatial distribution of the resistive zone (R1) and unit C is consistent (Fig. 11(a)). Therefore, we can assume that the basement rock of the Ikurushibe or older formations is distributed on the south-western side of the 1938 fault zone. The area between 500 and 1000 m under site 10a shows relatively low resistivity. This conductive zone may indicate an older formation underlying the Ikurushibe formation or sediments within the Ikurushibe formation (Matsunami and Yahata, 1989), which generally shows low resistivity compared to andesites (NEDO, 1985).

The low Bouguer anomaly in the Kutcharo caldera can be explained by the thick sediment (units A-1, B; Fig. 3). The low to moderate resistivity zone (10–200 ohm-m), including the C2 conductor north-east of R1, corresponded to units A-1 and B that were inferred as the sediment-fill-covered Kutcharo caldera (Fig. 11(a)). Based on the hypothetical testing discussed in 3.4, the R1 margin was most likely located between S-2 and S-4, and a sharper resistivity boundary may have been distributed there than indicated by the inverted resistivity model. These features are consistent with the steep incline zone of the density boundary between units B and C, and indicate that the resistivity and density distributions image the geological boundary of past caldera activities.

5.2 The relationship between the 1938 Kutcharo earthquake and the Kutcharo caldera

The detailed resistivity image produced by the DC electric survey data suggests cumulative fault activity in the Quaternary along the 1938 rupture zones (Fig. 10). The density model constrained by boreholes TS-3, TS-6, and TS-1 showed a steeply dipping boundary between units B and C beneath this area (Fig. 3). The resistivity section obtained from the MT data also supports this boundary (Figs. 7, 11(a)). In general, many inland earthquakes are the result of an abrupt slip within large discontinuous zones. Therefore, this clear spatial correspondence between the main depression boundary of the Kutcharo caldera and the 1938 fault indicates that an abrupt slip along the caldera margin caused the 1938 earthquake.

Normal faulting with the collapse of the caldera, the release of regional stress due to a crustal heterogeneity and fluid intrusion are three possible mechanisms for the 1938 earthquake. The first possibility is unlikely because depression (outer sides) and upheaval (inner sides) of the caldera occurred after the 1938 earthquake and were based on changes in the lake-water level (Tsuya, 1938; Kato, 1940; Fig. 1(c)). In addition, the 1938 earthquake caused left-lateral strike-slip displacement.

The second possibility may be appropriate because large contractive strain (about 8 ppm during 1883–1994) has been

accumulating in the eastern Hokkaido area (Hashimoto and Tada, 1988) generated by the oblique subduction of the Pacific plate along the Kurile trench. As Table 1 shows, geological differences between the caldera fill (units A and B) and basement rock (unit C) create a clear elastic boundary (Young's modulus). Generally, the local elastic heterogeneity in the regional-stress field induces a localised accumulation of stress resulting in fault ruptures. Many inland earthquakes were explained by this theory (e.g. Iio and Kobayashi, 2002; Ichihara *et al*., 2008). The 1938 earthquake was a release of accumulated regional stress around an area of strong elastic heterogeneity due to the caldera structure; however, the north-west–south-east azimuth of the contractive axis is nearly parallel to the strike azimuth of the 1938 fault. Thus, the small shear stress is believed to have induced fault slip.

The third possibility is that fluid injection from associated magma activity induced or enhanced the 1938 earthquake. Fluid injection can directly cause fault rupture as discussed by Julian (1983). He indicated that a dyke intrusion along or near the vertical fault plane of the Long Valley caldera caused several M 6 earthquakes. This hypothesis is based on mechanisms that cannot be explained by a double-couple mechanism, but can be explained by a compensated linear-vector dipole mechanism induced by dyke intrusion. Savage and Cockerham (1984) obtained a corresponding source model from geodetic surveys. No specific seismic and geodetic studies have been conducted in the Teshikaga area; however, magma intrusion relating to the 1938 earthquake is supported by the following points. First, the depression boundary beneath the rupture zone can easily become a pathway of intrusion. Second, the C1 conductor, which indicates hydrothermal activity beneath the depression boundary, suggests the presence of magma activity.

Fluid injection can also enhance double-couple earthquakes. High-pressure fluid injection into the fault plane of the San Andreas Fault reduced shear-fracture strength and allowed fault slip in the small shear-stress environment (e.g., Rice, 1992; Sasai, 1997). The high-pressure fluid along the depression boundary of the 1938 fault is consistent with this notion because the C1 montmorillonite-rich zone could behave as an impermeable cap for the supplied fluids transported through the 1938 fault plane (Nurhasan *et al*., 2006). Thus, the 1938 earthquake may have resulted from a similar mechanism as described for the San Andreas Fault. Consequently, the mechanism for the earthquake around the Kutcharo caldera can be explained by the fluid intrusion hypothesis. This mechanism and stress accumulation due to crustal heterogeneity do not conflict, and thus could have acted synergistically to induce the 1938 earthquake. A dense seismicity and geodetic network around the caldera is expected to contribute to the understanding of the complex relationship between fluid behaviour and earthquake occurrence.

6. Conclusion

Density and resistivity structures were investigated around the seismogenic zone of the 1938 Kutcharo earthquake (M 6.0) to identify the relationships between the earthquake and the caldera structure. The final density model revealed a highly inclined geological boundary corresponding to a main depression-zone margin in the Kutcharo caldera that was underneath the estimated fault. The bottom of the caldera was inferred to be over 3.5 km deep. The resistivity structure, derived from AMT surveys, supported the geological boundary at the depression boundary. A detailed resistivity section, revealed by a DC electric survey, showed discontinuities under the rupture zone, indicating cumulative vertical displacement generated by fault activity. The discontinuity seemed to extend to the depression boundary. Therefore, the 1938 earthquake probably resulted from fault activity along the main depression margin of the Kutcharo caldera. We propose that the 1938 earthquake may have been caused by the collapse of the caldera as a result of normal faulting, the release of regional stress enhanced by a crustal heterogeneity, or fault rupture related to fluid intrusion. The first possibility was excluded because the depression and upheaval observed after the 1938 earthquake was inconsistent with the collapse of the caldera. The second possibility also seems unlikely because the maximum principal-stress axis and inferred fault strike are almost parallel. The last possibility suggests that fluid intrusion induced a compensated linear-vector dipole mechanism into the dyke. This high-pressure intrusion into the fault reduced fracture strength and allowed fault-slip due to small shear stress. However, little evidence exists to support these mechanisms. Thus, stationary seismic and geodetic observations are needed around the Kutcharo caldera.

Acknowledgments. We thank Prof. Yasuo Ogawa of the Tokyo Institute of Technology and Prof. Masaaki Mishina of Tohoku University for providing many of the instruments used in the MT survey. We also thank landowners in the study region for allowing us to establish observation sites on their land. The editor, Dr. Akira Takada, and two reviewers, Prof. Yoichi Sasai and another anonymous reviewer, helped us to improve the manuscript. Helpful discussions with Prof. Takeshi Hashimoto, Prof. Yasunori Nishida, Dr. Ryo Honda, Dr. Hiroaki Kamiyama and Prof. Hiroaki Takahashi of Hokkaido University helped improve the content of this paper. GMT software (Wessel and Smith, 1998) was used to draw some of the figures.

References

Archie, G. E., The electrical resistivity log as an aid in determining some reservoir characteristics, *Transactions of the American Institute of Mining, Metallurgical and Petroleum Engineers*, **146**, 54–62, 1942.

Caldwell, T. G., H. M. Bibby, and C. Brown, The magnetotelluric phase tensor, *Geophys. J. Int.*, **158**, 457–469, 2004.

Geographical Survey Institute, Crustal deformations around Atosanupuri volcano, *Report of Coordinating Committee for Prediction of Volcanic Eruption*, **91**, 1–4, 2006 (in Japanese).

Hasegawa, K., A. Yamamoto, H. Kamiyama, and M. Nakagawa, Gravity structure of the Akan caldera and its vicinity, eastern Hokkaido, Japan, *Geophys. Bull. Hokkaido University*, **69**, 97–112, 2006 (in Japanese with English abstract).

Hashimoto, M. and T. Tada, Horizontal crustal movements in Hokkaido and their tectonic implications, *Zisin 2*, **41**, 29–38, 1988 (in Japanese with English abstract).

Hill, D. P., J. O. Langbein, and S. Prejean, Relations between seismicity and deformation during unrest in Long Valley caldera, California, from 1995 through 1999, *J. Volcanol. Geotherm. Res.*, **127**(3–4), 175–193, 2003.

Hirose, W. and M. Nakagawa, K-Ar ages of the Neogene volcanic rocks from the Kutcharo caldera region, east Hokkaido, with special reference to the Quaternary volcanic history, *J. Geol. Soc. Jpn.*, **101**, 99–102, 1995 (in Japanese with English abstract).

Ichihara, H., T. Mogi, Y. Yamaya, H. Kamiyama, and Y. Ogawa, Crust structure at Teshikaga region, eastern Hokaido, demonstrated by wide-band magnetoteluric and gravity surveys, *Geophys. Bull. Hokkaido University*, **69**, 233–255, 2006 (in Japanese with English abstract).

Ichihara, H., R. Honda, T. Mogi, H. Hase, H. Kamiyama, Y. Yamaya, and Y. Ogawa, Resistivity structure around the focal area of the 2004 Rumoi-Nanbu earthquake (M 6.1), northern Hokkaido, Japan, *Earth Planets Space*, **60**, 883–888, 2008.

Iio, Y. and Y. Kobayashi, A physical understanding of large intraplate earthquakes, *Earth Planets Space*, **54**, 1001–1004, 2002.

Jackson, J. A., Reactivation of basement faults and crustal shortening in orogenic belts, *Nature*, **283**, 343–346, 1980.

Japan Geothermal Energy Development Centre, A Basic Report for Geothermal Development no. 18, Atusa-nupuri, 103 pp., 1980 (in Japanese).

Julian, B. R., Evidence for dyke intrusion earthquake mechanisms near Long Valley caldera, California, *Nature*, **303**, 323–325, 1983.

Kato, A., S. Sakai, N. Hirata, E. Kurashimo, T. Iidaka, T. Iwasaki, and T. Kanazawa, Imaging the seismic structure and stress field in the source region of the 2004 mid-Niigata Prefecture earthquake: structural zones of weakness and seismogenic stress concentration by ductile flow, *J. Geophys. Res.*, **111**, doi:10.1029/2005JB004016, 2006.

Kato, Y., Investigation of the changes in the Earth's magnetic field accompanying earthquakes or volcanic eruptions, 2nd report: on the strong earthquake of May 29th 1938, which occurred near Kuttyaro Lake, Hokkaido, *Science Reports of the Tohoku Imperial University*, **1**, 19, 315–328, 1940.

Katsui, Y., Geological map of Japan, "Kutcharo-ko" with explanatory text, 1–42, Geological Survey of Japan, 1962 (in Japanese with English abstract).

Koshimizu, S. and J. Ikushima, Fission-track dating of the Older Kutcharo pyroclastic flow (Furume welded tuff) in eastern Hokkaido, Japan, *J. Geol. Soc. Jpn.*, **95**, 77–79, 1989 (in Japanese with English abstract).

Koshimizu, S. and C. W. Kim, Fission-track dating of the Cenozoic formations in central-eastern Hokkaido, Japan (part III): "green tuff" in eastern zone, *J. Geol. Soc. Jpn.*, **92**, 871–878, 1986 (in Japanese with English abstract).

Ledo, J., P. Queralt, A. Marti, and A. G. Jones, Two-dimensional interpretation of three-dimensional magnetotelluric data: an example of limitations and resolution, *Geophys. J. Int.*, **150**, 127–139, 2002.

Matsunami, T. and M. Yahata, Geothermal resources of the Teshikaga area, east Hokkaido, part 1—Conceptual model of geothermal system—, *Report of the Geological Survey of Hokkaido*, **60**, 35–76, 1989 (in Japanese with English abstract and captions).

Mori, J. and C. McKee, Outward-dipping ring-fault structure at Rabaul caldera as shown by earthquake locations, *Science*, **235**, 193–195, 1987.

Murata, Y., Estimation of optimum average surficial density from gravity data: an objective Bayesian approach, *J. Geophys. Res.*, **98**, 12097–12109, 1993.

NEDO, Report of Geothermal Development Promotion Project No. 6, Western Teshikaga region, 554 pp., 1985 (in Japanese).

Nurhasan, Y. Ogawa, N. Ujihara, S. B. Tank, Y. Honkura, S. Onizawa, T. Mori, and M. Makino, Two electrical conductors beneath Kusatsu-Shirane volcano, Japan, imaged by audiomagnetotellurics, and their implications for the hydrothermal system, *Earth Planets Space*, **58**, 1053–1059, 2006.

Ogawa, Y. and T. Uchida, A two-dimensional magnetotelluric inversion assuming Gaussian static shift, *Geophys. J. Int.*, **126**, 69–76, 1996.

Park, S. K. and B. Wernicke, Electrical conductivity images of Quaternary faults and Tertiary detachments in the California Basin and Range, *Tectonics*, **22**, doi:10.1029/2001TC001324, 2003.

Prejean, S., A. Stork, W. Ellsworth, D. Hill, and B. Julian, High precision earthquake locations reveal seismogenic structure beneath Mammoth Mountain, California, *Geophys. Res. Lett.*, **30**, doi:10.1029/2003GL018334, 2003.

Rice, J. R., Fault stress states, pore pressure distributions, and the weakness of the San Andreas Fault, in *Earthquake Mechanics and Transport Properties of Rocks*, edited by Evans, B. and T. F. Wong, 475–503, Academic Press, 1992.

Sasai, Y., Monitoring of the fluid-driven earthquakes by means of electromagnetic observations, *Proceeding of CA Symposium (1997)*, 37–44, 1997 (in Japanese).

Satoh, H., Y. Nishida, Y. Ogawa, M. Takada, and M. Uyeshima, Crust and upper mantle resistivity structure in the southwestern end of the Kuril Arc as revealed by the joint analysis of conventional MT and network MT data, *Earth Planets Space*, **53**, 829–842, 2001.

Savage, J. C. and R. S. Cockerham, Earthquake swarm in Long Valley caldera, California, January 1983—evidence for dike inflation, *J. Geophys. Res.*, **89**, 8315–8324, 1984.

Siripunvaraporn, W., G. Egbert, and M. Uyeshima, Interpretation of two-dimensional magnetotelluric profile data with three-dimensional inversion: synthetic examples, *Geophys. J. Int.*, **160**, 804–814, 2005.

Suzuki, K., S. Toda, K. Kusunoki, Y. Fujimitsu, T. Mogi, and A. Jomori, Case studies of electrical and electromagnetic methods applied to mapping active faults beneath the thick quaternary, *Engineering Geology*, **56**, 29–45, 2000.

Suzuki, S. and T. Hirota, Seismic activity in the eastern part of Hokkaido and its vicinity—shallow earthquakes in Teshikaga-Akan area, *Zisin 2*, **26**, 77–92, 1973 (in Japanese with English abstract).

Takakura, S., Resistivity of Neogene rocks in the Niigata and the Akita oil fields, Japan, *Geophys. Explor. (Butsuri-Tansa)*, **48**, 161–175, 1995.

Talwani, M., J. L. Worzel, and M. Landisman, Rapid gravity computation for two-dimensional bodies with application to the Mendocino Submarine Fracture Zone, *J. Geophys. Res.*, **64**, 49–59, 1959.

Tanakadate, S., 1938 Kutcharo earthquake, part 1, *Zisin 1*, **10**, 529–542, 1938 (in Japanese).

Tsuya, H., An investigation report of the May 29, 1938, Kutcharo earthquake, *Zisin 1*, **10**, 285–313, 1938 (in Japanese).

Uchida, T., Two-dimensional resistivity inversion for Schlumberger sounding, *Geophys. Explor. (Butsuri-Tansa)*, **44**, 1–17, 1991.

Umino, N., T. Matsuzawa, S. Hori, A. Nakamura, A. Yamamoto, A. Hasegawa, and T. Yoshida, 1996 Onikobe earthquakes and their relation to crustal structure, *Zisin 2*, **51**, 253–264, 1998 (in Japanese with English abstract).

Wessel, P. and W. H. F. Smith, New, improved version of the Generic Mapping Tools released, *EOS Trans. AGU*, **79**, 579, 1998.

Wight, D. E. and F. X. Bostick, Cascade decimation—a technique for real time estimation of power spectra, *Proceedings of the IEEE International Conference on Acoustic Speech Signal Processing*, 626–629, 1980.

Yamamoto, A. and H. Ishikawa, Gravity anomaly in the eastern part of Hokkaido, Japan, *Geophys. Bull. Hokkaido University*, **67**, 285–309, 2004 (in Japanese with English abstract and captions).

Yokoyama, I., Gravity survey on Kuttyaro Lake, *J. Phys. Earth*, **6**, 75–79, 1958.

H. Ichihara (e-mail: h-ichi@eri.u-tokyo.ac.jp), T. Mogi, H. Hase, T. Watanabe, and Y. Yamaya